

Structural And Magnetic Properties Of Spinel Mg-Ni Ferrites Nanoparticles Synthesized By Microwave Combustion Method

P. Antony Lyla^{1*}, and E. Thirumal²

^{1*} Research scholar, Department of Physics, Bharath Institute of Higher Education and Research (BIHER), Chennai - 600073

² Professor, Department of Physics, Bharath Institute of Science and Technology (BIST), Chennai – 600073

lylalenin@gmail.com (P. Antony Lyla)

esthirumal@gmail.com (E. Thirumal)

Article History Received: 10 January 2021; Revised: 12 February 2021; Accepted: 27 March 2021; Published online: 28 April 2021

Abstract

Magnesium (Mg^{2+}) ions doped nickel ferrite ($NiFe_2O_4$) nanoparticles with the general formula $Mg_xNi_{1-x}Fe_2O_4$ ($y = 0.0$ and 0.5) was synthesized by microwave combustion method, using urea as the fuel. Phase identification and structural parameters were analyzed by X-ray powder diffraction (XRD). Mg^{2+} doping concentration in $NiFe_2O_4$ greatly affected the size of the crystallite and obtained the size ranges from 22.5nm - 24.8 nm and all the samples show a single cubic spinel structure without any secondary step. For increased the concentration of Mg^{2+} doping, the lattice parameters are decreased, while decreasing trend has been observed in the case of particle size, which was confirmed by HR-SEM analysis. The influence of non-magnetic nature of Mg^{2+} doping on $NiFe_2O_4$ and replaces the magnetic nature of Ni^{2+} ions, which changes their magnetic properties and were studied under the applied field 15 kOe. The overall results showed that even a small amount of Mg^{2+} doping changes the structural and magnetic properties of the spinel $NiFe_2O_4$ nanoparticles.

Keywords: Magnetic nanoparticles; Spinel $NiFe_2O_4$; Microwave combustion; Magnetic properties.

1. Introduction

Recently, tertiary mixed metal oxides with cubic spinel structure nanoparticles, due to their exceptional physicochemical, mechanical, magnetic, and dielectric properties, have the most promising materials for electrochemical energy storage activities, televisions, transformers, magnetic recording devices, biomedical applications, etc. [1-4]. The general equation of cubic spinel structure is AB_2O_4 , where bivalence metal particles 'A' and trivalence metal particles 'B' [5]. The spinel ferrite precious stone structure comprises of a cubic-shut course of action of oxygen particle with 8 tetrahedral (A-site) and 16 octahedral interstitials (B-site) destinations in the unit cell [6,7]. In this way, in the spinel ferrites, a gigantic segment of empty A and B positions were accessible to move cations between the interstitial locales [8]. The ordinary spinel structure happens with the wide control of tetrahedral (A) locales with M^{2+} (divalent metal cations), though living of octahedral destinations [B] completely Fe^{3+} particles yield the converse spinel structure with bivalence metal cations involve in both A and B locales on account of blended spinel structure [9,10].

In the previous decades, the union of nano-sized materials has been expanded to locate an unassuming, stable, and viable procedure for controlling their auxiliary parameters with a higher explicit surface region [11,12]. The size-subordinate ferrite particles with cubic spinel structure were amazing materials planned in ongoing decades with extraordinary physicochemical properties [13]. The cubic spinel ferrite tempts inquire about significance because of exceptional, adaptable, and distinctive field applications. Nickel ferrite were novel innovatively solid among all cubic spinel ferrite materials, appropriate for an assortment of uses in water parting, biomedical, photocatalysts, transformer center, microwave, attractive account media, and gas sensor [14,15].

The spinel ferrites physicochemical, electrical, and attractive properties are recognizably influenced by the expansion of the cations and their particular dispersal among the tetrahedral and octahedral interstitial destinations [16]. Just as the extraordinary degree by changing the planning strategy and diminishing molecule size when the material is in the nano size. These properties are progressively exceptional to contemplate strategies, calcination temperature, compound structure, and assortment and convergence of the dopants [17,18].

Only the spinel ferrites, $NiFe_2O_4$ is the furthestmost inquisitive assets because of their honorable synthetic dependability, upstanding reactant and optical properties, modest, and calm mechanical advancement, they are utilized positively in the microwave enterprises [19]. Generally, $NiFe_2O_4$ is a delicate attractive material with uncommon physical, concoction, electrical and attractive properties, and these properties for the most part reliant on

Fe^{2+} and Fe^{3+} particles change, moreover, the trade of tri-valence metal particles in the zinc ferrite were quick to show the physicochemical, attractive, and electrical properties [20]. Mg-doped NiFe_2O_4 were considered delicate attractive material inferable from their oversimplified mix of Mg particles in the unit cell of NiFe_2O_4 because of the practically equivalent to estimate of Fe^{3+} particle [21]. In current days, nanoparticles of spinel ferrite were combined by various systems, for example, concoction co-precipitation, microwave, sol-gel technique [22-25], and so forth.

In present work, the combination of Mg-doped NiFe_2O_4 has arranged by microwave burning strategy. It is a beneficial, modest, and basic surfactant-helped synthetic procedure to yield an enormous amount of littler molecule size with favored structure, chain of importance, and furthermore wanted natural organization at a lower sintering temperature when contrasted with the customary clay strategy.

2. Experimental part

2.1. Materials and methods

Nickel nitrate ($\text{Ni}(\text{NO}_3)_2 \cdot 6\text{H}_2\text{O}$, 98%), Magnesium nitrate ($\text{Mg}(\text{NO}_3)_2 \cdot 6\text{H}_2\text{O}$, 98%), Ferric nitrate ($\text{Fe}(\text{NO}_3)_3 \cdot 9\text{H}_2\text{O}$, 98%) and urea ($\text{CO}(\text{NH}_2)_2$) were utilized as a fuel for this response. The syntheses of unadulterated and Mg-doped NiFe_2O_4 were set up with the expansion of magnesium cations of various molar proportions ($\text{Mg}_x\text{Ni}_{1-x}\text{Fe}_2\text{O}_4$ with $x = 0.0$ and 0.5) to NiFe_2O_4 . For the synthesis of NiFe_2O_4 utilizing the microwave system, the antecedent's blend in urea, was set into microwave and presented to the microwave vitality in a 2.45 GHz multimode pit at 850 W for 15 min. Metal nitrate salts and urea arrangement will be picked by thinking about the decreasing and oxidizing specialist valences of the crude materials and were measured in comparability of NOx decrease (N_2O to N_2 , CO_2 and H_2O) at a low temperature. The response in the microwave depression was planned because of the way that urea has a high dielectric misfortune esteem, which will be warmed quick in the microwave warming framework. After fulfillment of the response, the strong powder was gotten and after that washed with ethanol and dried at 80°C for 30 minutes. The got powders were marked as NiFe_2O_4 and $\text{Mg}_{0.5}\text{Ni}_{0.5}\text{Fe}_2\text{O}_4$.

2.2. Characterization techniques

The auxiliary portrayal of unadulterated and Mg-doped NiFe_2O_4 was performed utilizing a Philips X'pert X-beam diffractometer (XRD) with Cu-K α radiation at $\lambda = 1.540 \text{ \AA}$. Morphological investigations and vitality dispersive X-beam examination (EDX) of unadulterated and Mg-doped NiFe_2O_4 have been performed with a Jeol JSM6360 high goals filtering electron magnifying lens (HR-SEM). Attractive estimations were done at room temperature utilizing a PMC MicroMag 3900 model vibrating test magnetometer (VSM) furnished with 1 Tesla magnet.

2.3. Photocatalytic experiments

Photocatalytic corruption of methylene blue (MB) color was utilized to look at the photocatalytic capability of unadulterated and Mg-doped NiFe_2O_4 nano-photocatalysts. The UV light was situated at 5-cm good ways from the arrangement surface. In the wake of including the unadulterated and Mg-doped NiFe_2O_4 nano-photocatalysts to a MB arrangement, it was blended precisely for 20 minutes in obscurity for adsorption balance response. Other UV lights were utilized to illuminate the arrangement, and the reactor substance were blended in a mechanical stirrer. It ought to be noticed that all analyses were done at encompassing temperature. For keeping a steady temperature, we set the reactor in a cooling chamber. During illumination, the examples were gathered at explicit interims and inspected by HPLC after photocatalyst partition by an outer magnet.

3. Results and discussion

3.1. X-ray diffraction analysis

Figure 1 uncovers the X-beam diffraction examples of spinel $\text{Mg}_x\text{Ni}_{1-x}\text{Fe}_2\text{O}_4$ ($x = 0.0$ and 0.5) samples. All XRD peaks were coordinated with the JCPDS card numbers 89-1012, which confirmed the formation of spinel NiFe_2O_4 . The key diffraction planes are (111), (220), (311), (222), (400), (422), (511), (440), and (531) by most extraordinary diffraction pinnacle recognized for plane (311) clearly affirms the exactness of cubic spinel structure. The grid steady (a) remained intentional by means of condition (1).

$$a = d (h^2 + k^2 + l^2)^{1/2} \quad (1)$$

where h, k, and l are Miller records of the precious stone planes and d is bury organizer separation for hkl planes. The estimation of 'a' was barely diminishes with an expansion in Mg focus level because of the distinction in the ionic size of Mg^{2+} (0.615 \AA) and Ni^{2+} (0.645 \AA), and it unmistakably adheres to Vegard's law [26].

The D_{XRD} (normal crystallite size) of test powders were considered by methods for Debye-Scherrer recipe:

$$D_{\text{XRD}} = \frac{0.89\lambda}{\beta \cos\theta} \quad (2)$$

Where, λ represents an episode wavelength of X-beam source Cu-K α radiation, β represents FWHM (full-width at half greatest) in radians in the 2θ scale, θ is the Bragg edge, D_{XRD} is crystallite size in nm. To discover β and θ

values for all examples, the Gaussian fitting model was embraced. The molecule size of the examples were expanded because of the substitution of Mg^{2+} ions having a littler sweep than of Ni^{2+} cations. The D_{XRD} (crystallite size) increments from 22.5 - 24.8 nm with the expansion in the Mg^{2+} ions ($x = 0.0 - 0.5$).

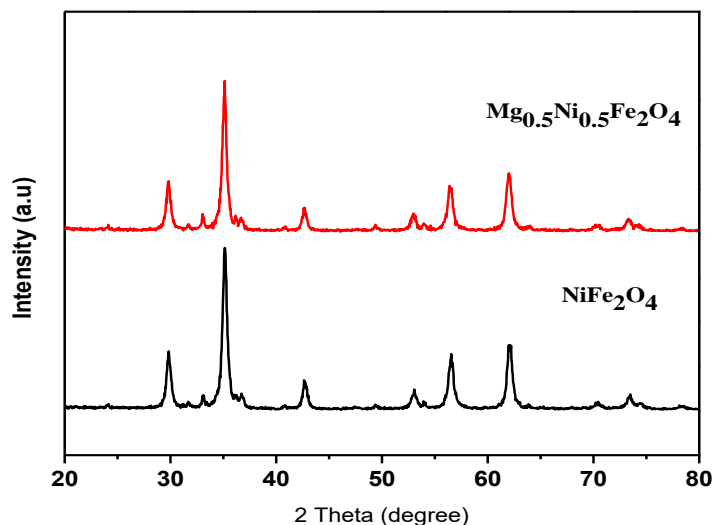


Figure 1. Powder XRD patterns of Pure and Mg-doped $NiFe_2O_4$ nanoparticles.

Table 1. Crystallite size (D), and lattice parameter, (a) values of Mg-doped $NiFe_2O_4$ nano-photocatalysts.

Sl. No.	Samples	Crystallite size (nm)	Lattice parameter (Å)
1.	$NiFe_2O_4$	28.58	8.288
2.	$Mg_{0.5}Ni_{0.5}Fe_2O_4$	25.36	8.256

3.2. FT-IR analysis

The FT-IR spectra give the data about central changes and to affirm the tetrahedral and octahedral locales of spinel ferrites. It likewise affirms the debasement states and concoction substances related with particles surface.

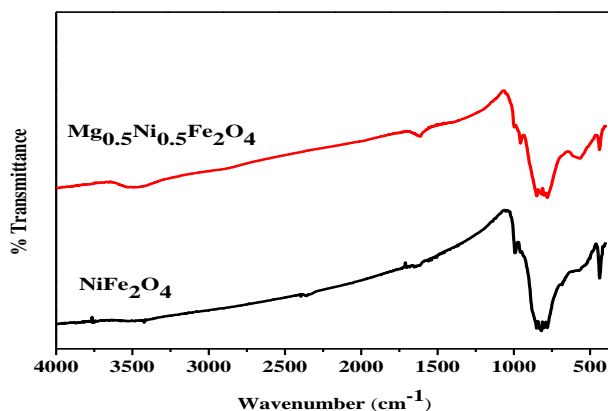
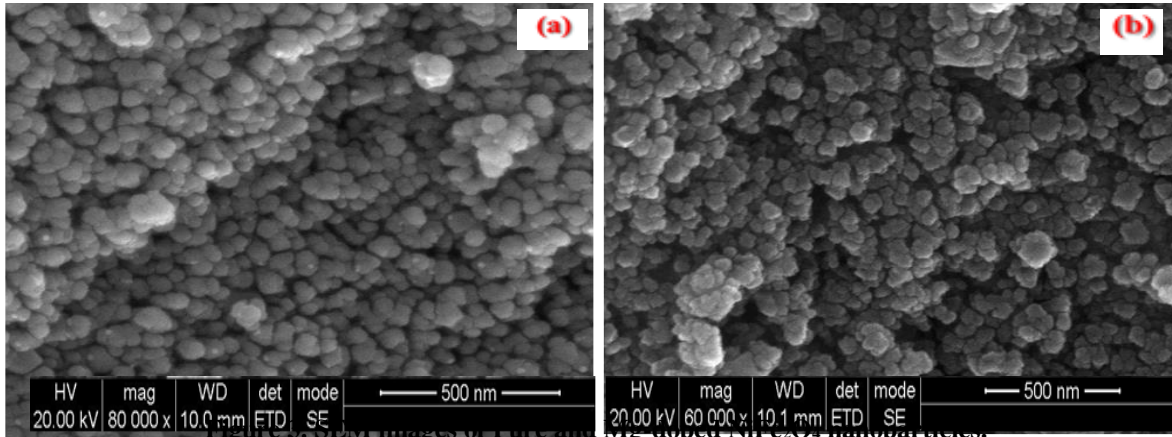


Figure 2. FT-IR spectra of Pure and Mg-doped $NiFe_2O_4$ nanoparticles.

Fig. 2 shows the transmittance spectra portrayed two fundamental wide metal-oxygen groups in the middle of 400–600 cm^{-1} demonstrates the development of unadulterated and Mg-doped NiFe_2O_4 cubic spinel [27]. The higher wave number ν_1 ingestion band started by expanding vibration of the tetrahedral metal-oxygen, by and large saw in the middle of 544-569 cm^{-1} and lower wave number ν_2 retention band was in the middle of 432-439 cm^{-1} for octahedral metal-oxygen vibrational extending. The retention groups at 439 cm^{-1} and 569 cm^{-1} were for octahedral and tetrahedral destinations of nickel ferrite [28].

3.3. Morphological analysis

The HR-SEM pictures for spinel $\text{Mg}_x\text{Ni}_{1-x}\text{Fe}_2\text{O}_4$ ($x = 0.0$ and 0.5) samples were exhibited in Fig. 3(a-d). From Fig. 3, an about uniform and agglomerated grains were watched. The morphology and size of particles were affected by the substitution of Mg^{2+} ions. The remarkable increase in the Mg^{2+} ions changes the molecule size and it increases from 25 - 28 nm which is bigger than D_{XRD} .



3.4. Elemental analysis

The elemental composition analysis of spinel $\text{Mg}_x\text{Ni}_{1-x}\text{Fe}_2\text{O}_4$ ($x = 0.0$ and 0.5) samples was explored by EDX strategy. Fig. 4 speaks to the EDX charts for the $\text{Mg}_x\text{Ni}_{1-x}\text{Fe}_2\text{O}_4$ ($x = 0.0$ and 0.5) samples. It plainly inspects the homogeneity of the readied tests and polluting influences related with synthetic structure during the blend procedure. The compositional level of iron, nickel, magnesium, and oxygen components in $\text{Mg}_x\text{Ni}_{1-x}\text{Fe}_2\text{O}_4$ ($x = 0.0$ and 0.5) samples was noted and confirmed their purity of the final products.

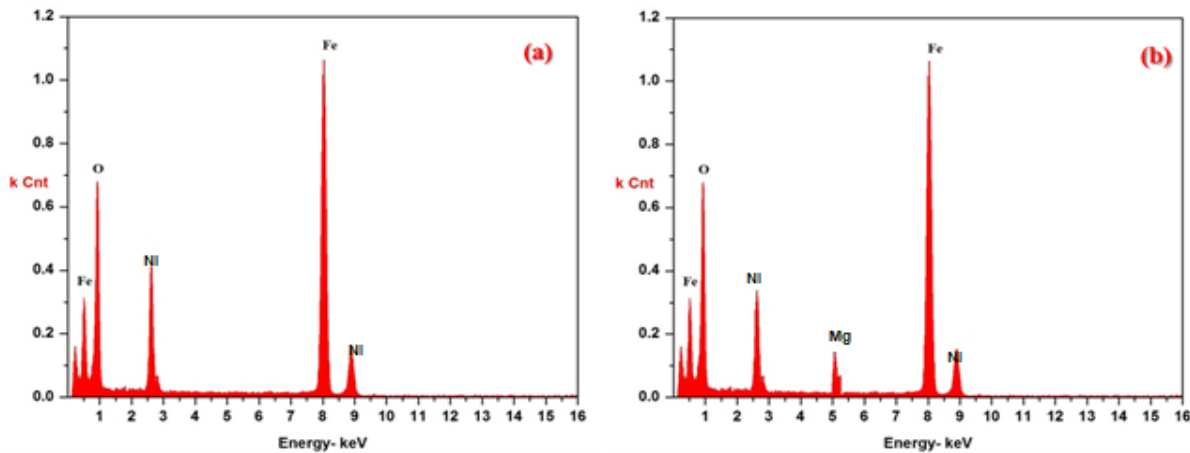


Figure 4. EDX analysis of Pure and Mg-doped NiFe_2O_4 nanoparticles.

3.5. Magnetic analysis

The room temperature bends of magnetization versus the applied field (M-H circles) for spinel $\text{Mg}_x\text{Ni}_{1-x}\text{Fe}_2\text{O}_4$ ($x = 0.0$ and 0.5) samples tests are appeared in Fig. 5. For all samples, the magnetization arrived at immersion at an attractive field of 15 KOe. The attractive properties were resolved utilizing Fig. 5 and all qualities are exhibited in Table 2. The saturation magnetization (M_s) saying as stretched out essentially with the expansion of

Mg²⁺ ions. For spinel Mg_xNi_{1-x}Fe₂O₄, when x worth was expanded from 0.0 to 0.5, the Ms esteem likewise stretched out. For the most part the Mg²⁺ ions replaces the Ni²⁺ ions in tetrahedral locales, diminishing the attractive snapshot of Mg_xNi_{1-x}Fe₂O₄ at lower doping fixation. Hc qualities are unmistakably influenced by Mg_xNi_{1-x}Fe₂O₄ substitution. From Table 2, it is seen that Hc worth was diminished with increment in Mg²⁺ ions focus while expanded for y = 0.0, 0.5 samples. As detailed the Mg²⁺ ions -doped NiFe₂O₄ test has the most elevated coercivity esteem, which was because of the molecule size impact, nature of dopant, and higher doping focus [29, 30].

Figure 5. VSM analysis of Pure and Mg-doped NiFe₂O₄ nanoparticles.

Table 2. Magnetic properties (H_c, M_r and M_s) of pure and Mg-doped NiFe₂O₄ nano-photocatalysts.

Sl. No.	Samples	H _c (Oe)	M _r (emu/g)	M _s (emu/g)
1.	NiFe ₂ O ₄	9.45	0.885	56.48
2.	Mg _{0.5} Ni _{0.5} Fe ₂ O ₄	7.28	0.745	42.55

3.6. Photocatalytic properties

The crystallinity, size, doping metal ions, structure of the nano-catalysts are the significant factors, which are influence its photocatalytic performance. Surface area of the nanomaterials is very important for the photocatalytic activity. Jia et al. [31] reported the PCD efficiency of spinel ZnFe₂O₄ and obviously influence the surface properties and surface defects. Therefore, Mg doping Mg_xNi_{1-x}Fe₂O₄ (x = 0.0 and 0.5) samples and tune the PCD of MB dye. PCD efficiency of spinel NiFe₂O₄ is very low, and increased with rise in the Mg doping at x = 0.5 (Mn_{0.5}Ni_{0.5}Fe₂O₄), due to the higher surface area of Mn_{0.5}Ni_{0.5}Fe₂O₄ NPs. Besides, as the particle size decreases, the number of active surface sites increased. Therefore, it is believed that the high surface area of Mn_{0.5}Ni_{0.5}Fe₂O₄ NPs could enhance the photocatalytic properties than that of other samples [32].

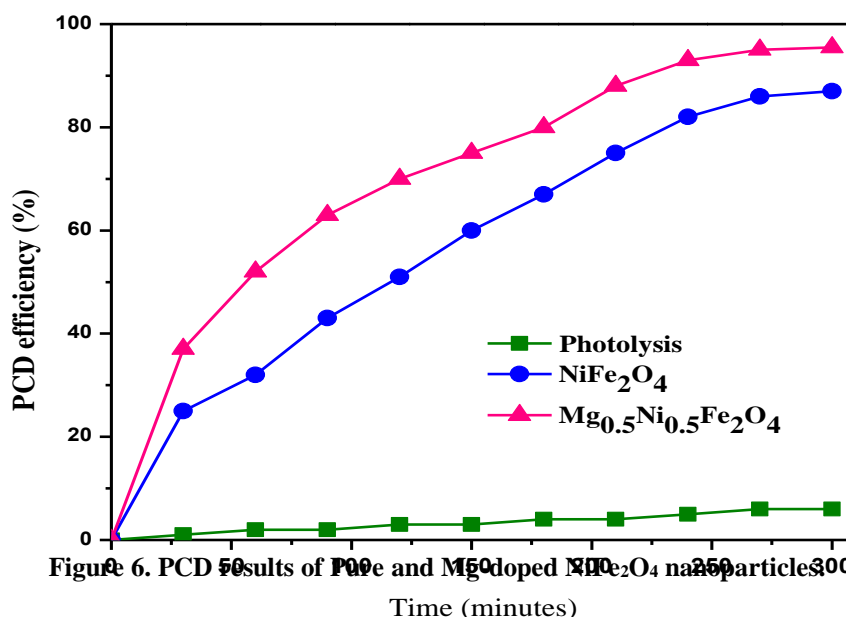


Figure 6. PCD results of Pure and Mg-doped NiFe₂O₄ nanoparticles.

Table 3. PCD percentage for the degradation of MB dye.

SL. No.	Samples	PCD efficiency (%)
1.	NiFe ₂ O ₄	89.58
2.	Mg _{0.5} Ni _{0.5} Fe ₂ O ₄	96.84

4. Conclusions

In the present investigation, we delivered compositionally changed nanoparticles of spinel $Mg_xNi_{1-x}Fe_2O_4$ ($x = 0.0$ and 0.5) samples by devouring profoundly dissolvable nitrate salts of iron, nickel, and magnesium with urea through microwave combustion method. The XRD results demonstrated that the crystallite size increments in the range $\sim 22\text{--}28$ nm with the substitution of Mg^{2+} single cubic spinel structure in $NiFe_2O_4$. Moreover, resultant changes were explored by FTIR in the bond extending vibration of tetrahedral and octahedral metal buildings appeared in the scope of $400\text{--}600\text{ cm}^{-1}$. Undoped $NiFe_2O_4$ auxiliary parameters causes certain deviations in skeletal and X-beam thickness, crystallite size, unit cell volume, and ionic length of the tetrahedral and octahedral destinations due to doping of Mg^{2+} ions in $NiFe_2O_4$. The HR-SEM micrographs uncovered that all samples were permeable game plan and about uniform shape with a normal molecule size $22\text{--}0.28$ nm. The impact of Mg^{2+} ions causes recognizable varieties in the basic, morphological, electrical, and attractive properties of spinel $Mg_xNi_{1-x}Fe_2O_4$ ($x = 0.0$ and 0.5) samples firmly rely upon the synthetic piece, size, and special dispersion of cations at (A) and (B) destinations.

References

1. K. Seevakan, A. Manikandan, P. Devendran, Y. Slimani, A. Baykal, T. Alagesan, *Ceramics International*, 44 (2018) 20075-20083.
2. J. Arul Hency Sheela, S. Lakshmanan, A. Manikandan, S. Arul Antony, *Journal of Inorganic and Organometallic Polymers and Materials* 28 (2018) 2388-2398.
3. M. Maria Lumina Sonia, S. Anand, V. Maria Vinosel, M. Asisi Janifer, S. Pauline, A. Manikandan, *Journal of Magnetism and Magnetic Materials*, 466 (2018) 238-251.
4. A.T. Ravichandran, J. Srinivas, A. Manikandan, A. Baykal, *Journal of Superconductivity and Novel Magnetism*, 32 (2019) 1663-1670.
5. A.D. Korkmaz, S. Güner; Y. Slimani, H. Gungunes, Md. Amir; A. Manikandan, A. Baykal, *Journal of Superconductivity and Novel Magnetism*, 32 (2019) 1057-1065.
6. A. Baykal, S. Guner, H. Gungunes, K.M. Batoo, Md. Amir, A. Manikandan, *Journal of Inorganic and Organometallic Polymers and Materials*, 28 (2018) 2533-2544,
7. Y. Slimani, A. Baykal, Md. Amir, N. Tashkandi, H. Güngüneş, S. Guner, H.S. El Sayed, F. Aldakheel, T.A. Saleh, A. Manikandan, *Ceramics International*, 44 (2018) 15995-16004
8. Md Amir, H. Gungunes, Y. Slimani, N. Tashkandi, H.S. El Sayed, F. Aldakheel, M. Sertkol, H. Sozeri, A. Manikandan, I. Ercan, A. Baykal, *Journal of Superconductivity and Novel Magnetism*, 32 (2018) 557-564.
9. A. Manikandan, M. Durka, S. Arul Antony, *J. Supercond. Nov. Magn.*, 28 (2015) 209-218.
10. K. Jeyabanu, P. Devendran, A. Manikandan, R. Packiyaraj, K. Ramesh, N. Nallamuthu, *Physica B: Condensed Matter*, 573 (2019) 92-101.
11. G. Mathubala, A. Manikandan, S. Arul Antony and P. Ramar, *J. Mol. Struct.*, 1113 (2016) 79-87.
12. A. Manikandan, E. Hema, M. Durka, K. Seevakan, T. Alagesan, S. Arul Antony, *J. Supercond. Nov. Magn.*, 28 (2015) 1783-1795.
13. E. Hema, A. Manikandan, M. Gayathri, M. Durka, S. Arul Antony, B. R. Venkatraman, *J. Nanosci. Nanotech.* 16 (2016) 5929-5943.
14. M. Maria Lumina Sonia, S. Anand, S. Blessi, S. Pauline, A. Manikandan, *Ceramics International*, 44 (2018) 22068-22079.
15. A. Manikandan, E. Manikandan, S. Vadivel, M. Kumaravel, D. Maruthamani, S. Hariganesh, *Photocatalysis: Present, past and future (Organic Pollutants in Wastewater-I Methods of Analysis, Removal and Treatment)*, Materials Research Foundations, 29 (2018) 34 Pages, DOI: <http://dx.doi.org/10.21741/9781945291630-7>
16. G. Padmapriya, A. Manikandan, V. Krishnasamy, S. K. Jaganathan, S. Arul Antony, *J. Supercond. Nov. Magn.*, 29 (2016) 2141-2149.
17. M. A. Almessiere, Y. Slimani, H. Gungunes, A. Manikandan, A. Baykal, *Results in Physics*, 13, (2019) 102166.
18. A. Manikandan, S. Arul Antony, R. Sridhar, Seeram Ramakrishna, M. Bououdina, *J. Nanosci. Nanotech.* 15 (2015) 4948-4960.
19. G. Mathubala, A. Manikandan, S. Arul Antony, P. Ramar, *Nanosci. Nanotech. Lett.* 8 (2016) 375-381.
20. K. Elayakumar, A. Dinesh, A. Manikandan, P. Murugesan, G. Kavitha, S. Prakash, R. Thilak Kumar, S. K. Jaganathan, A. Baykal, *Journal of Magnetism and Magnetic Materials*, 476 (2019) 157-165.

21. A. Manikandan, M. Durka, S. Arul Antony, *Adv. Sci., Eng. Med.*, 7 (2015) 33-46.
22. E. Hema, A. Manikandan, P. Karthika, M. Durka, S. Arul Antony, B. R. Venkatraman, J. *Nanosci. Nanotech.* 16 (2016) 7325-7336.
23. A. Manikandan, M. Durka, S. Arul Antony, *J. Supercond. Nov. Magn.*, 28 (2015) 2047–2058.
24. K. Seevakan, A. Manikandan, P. Devendran, Y. Slimani, A. Baykal, T. Alagesan, *Journal of Magnetism and Magnetic Materials*, 486 (2019) 165254.